Cell division protein A (CdpA) assembles and anchors the two FtsZ rings at midcell in haloarchaea

Yan Liao[1,#], Vinaya Devidas Shinde[1], Dalong Hu[1,2], Zhuang Xu[3], Bill Söderström[1], Katharine A. Michie[4], Iain G. Duggin[1,#]

1. Australian Institute for Microbiology & Infection, University of Technology Sydney, Australia
2. Saw SweeHock School of Public Health, National University of Singapore, Singapore
3. School of Mathematics and Statistics, The University of New South Wales, Australia
4. Structural Biology Facility, Mark Wainwright Analytical Centre, The University of New South Wales, Australia

Address correspondence to Yan Liao (yan.liao@uts.edu.au) and Iain Duggin (iain.duggin@uts.edu.au)

Abstract

Many archaea appear to divide through the coordinated activities of two distinct FtsZ homologues, FtsZ1 and FtsZ2, and another bacterial cell division homologue, SepF, which are part of the midcell division ring. Here, we discovered a novel cell division protein (HVO_0739, renamed CdpA) in *Haloferax volcanii*. CdpA represents the prototypical characterized member of a protein family widespread in Haloarchaea. Midcell division site localization of CdpA was dependent on the presence of the ring-assembly protein FtsZ1, and the division constriction protein FtsZ2 influenced the proper midcell assembly and structure of CdpA. In the absence of CdpA, cells frequently failed to divide properly and FtsZ1 and FtsZ2 were uncoupled from midcell, with FtsZ1 forming poorly condensed pseudo-helical structures, and FtsZ2 showing mispositioned foci and filaments that were often disorientated and perpendicular to the division ring along the cell edge. The dynamic movements of FtsZ1 and FtsZ2 clusters around the division ring were minimally affected by loss of CdpA, leading to dynamic repositioning of the aberrant FtsZ structures. In contrast, CdpA formed relatively immobile distinct foci around the ring. CdpA domain function studies, protein pull-down assays, and multimer structure predictions suggested that CdpA forms a central part of a membrane anchor complex that interacts with FtsZ2. CdpA has a transmembrane domain and a cytoplasmic disordered linker and small C-terminal domain, which appear to tether multiple division proteins to the midcell membrane. Our discovery of an archaeal FtsZ assembly and midcell anchor protein offers new insights into cell division mechanisms that are similar across the tree of life.

Introduction

Cell division is one of the most fundamental processes in all organisms. It is universally carried out through the localized assembly of cytoskeletal proteins into a ring-like structure linked to the cell membrane and envelope that initiates a constriction process leading to division. In most bacteria, the cytoskeletal protein FtsZ and other cytoskeletal and accessory proteins form the division ring that dynamically drives cell envelope constriction[1]. Bacterial FtsZ appears to perform multiple functions, including acting as scaffolding for protein recruitment to the division site, triggering membrane constriction[2, 3], and dynamically guiding cell wall synthesis to drive its inward growth[4, 5]. The relative contributions of these mechanisms to division *in vivo* are yet to be precisely defined. The eukaryotic homolog of FtsZ is tubulin, which greatly elaborates on the core polymerization function common to this superfamily of proteins, and forms microtubules that provide structural support and play essential roles in diverse cellular processes including intracellular transport and division, although tubulin is not considered a main component of the eukaryotic division ring. Multiple tubulin proteins exist in each species, with diversified and specialized functions to support the complex cellular events and differentiation processes that they underpin.

Most bacterial species contain only one FtsZ, but archaea, which are phylogenetically more closely related to eukaryotes, most commonly have two FtsZ homologues belonging to distinct families[6-8]. The dual-FtsZ system might resemble an early stage in the evolutionary diversification and specialization of cytoskeletal functions, as seen in eukaryotes. By using the archaeal model organism, *Haloferax volcanii*, previous work showed that they divide through the coordinated activities of FtsZ1 and FtsZ2[9, 10]. The role of archaeal FtsZ1 was primarily ascribed to promoting assembly of the midcell ring, whereas FtsZ2 was more directly implicated in the ring constriction process[10]. Thus, some of the multiple functions of bacterial FtsZ appear to be at least partially separated into specialized homologs in the archaeal dual-FtsZ system. Furthermore, FtsZ2 was found to be specifically absent in certain methanogenic archaea that—rarely in archaea—have a peptidoglycan (PG) cell wall, suggesting that FtsZ2 is needed for division when a PG wall is not present to support the inward growth of the cell envelope[10].

Current knowledge of FtsZ-based cell division in archaea is limited. There are only a few proteins in this system that have been identified and characterized, despite the many different components present in bacterial and eukaryotic cell division systems. In addition to the two FtsZ proteins, an archaeal homologue of the bacterial division protein SepF[11, 12] and the very recently reported PRC barrel domain proteins (CdpB1/2)[13, 14] were found to have roles in division. *H. volcanii* SepF associates with FtsZ2 at the division site and potentially the cell membrane[11], and CdpB1 also associates with SepF[13, 14]. Crystal structures and AlphaFold2 multimer predictions suggested a tripartite complex formed by CdpB1, CdpB2 and SepF, with CdpB1 and CdpB2 forming a polymer of alternating heterodimers[13]. Currently, there is very little information on what functions these proteins play in the division mechanism or how they are linked to the envelope at midcell.

Other expected components of the FtsZ-based archaeal divisome are yet to be identified, though candidate genes linked to cell division were identified on the basis that their expression or promoter regions were influenced by a transcriptional regulator that appears to control cell division, CdrS, which is encoded by a small ORF in an operon with *ftsZ2*[15, 16]. In *H. volcanii*, CdrS-regulated genes included *ftsZ1*, *ftsZ2*, *sepF*, *cdpB1* (Hvo_1691), and the diadenylate cyclase gene (*dacZ*) implicated in signal transduction and regulation of division[16, 17]. Another previously uncharacterized gene, HVO_0739, was, with *sepF*, amongst the most strongly regulated by CdrS[16]. Here we have determined the function HVO_0739, renaming the protein CdpA (Cell division protein A), and we propose the Cdp- prefix may be given to other haloarchaeal proteins when they are discovered to participate directly in the division mechanism. We applied genetic and protein structure-function analyses combined with high-resolution fluorescence microscopy to demonstrate the functions of CdpA in coupling the two FtsZ rings and anchoring them at the midcell for division.

Results

CdpA is conserved in haloarchaea and required for normal cell division in *H. volcanii*

We identified CdpA (HVO_0739) homologs encoded in 506 published archaeal genomes and performed a phylogenetic analysis of the amino acid sequences. The *cdpA* gene is typically present as a single gene in Haloarchaea, in which it co-exists with the two FtsZs (Fig. 1a) in 96.5% of the species analyzed. Based on protein topology and structure predictions (Fig. 1b), and a multiple sequence alignment (Supplementary Fig. 1), CdpA is comprised of three main regions: a conserved N-terminal transmembrane domain, a less conserved cytoplasmic disordered linker region, and a small cytoplasmic C-terminal domain. CdpA does not have a direct homolog in Bacteria or some of the more distantly related archaeal taxa, although we observed homologous CdpA-like proteins, which showed significant homology but differed in length ($\pm$ 20%) or number of N-terminal transmembrane segments ($\neq$ 4) compared to the reference CdpA (HVO_0739) in a diverse range of archaea (Fig. 1a). Some Halobacteriota species contained multiple homologs within the genome (Fig. 1a). For example, in *H. volcanii*, a CdpA-like protein (HVO_2016) with four predicted transmembrane segments lies adjacent to HVO_2015, which encodes an actin superfamily protein (volactin)[18] hinting of a potential common function associated with diverse cytoskeletal systems.

To identify the role of CdpA, we investigated the consequences of deleting the *cdpA* gene in *H. volcanii*. Microscopy revealed a cell division defect (Fig. 1c), where the Δ*cdpA* mutant showed a mixture of some greatly enlarged cells that had failed to divide and others with almost normal size. This great heterogeneity suggests an incomplete division defect where failure of cell division in some cells leads to enlarged cells that have a lower probability of division than the smaller cells, which further exaggerates their size defect. Consistent with this, time-lapse microscopy of growing Δ*cdpA* cells showed that some divided at mid-cell and others initially developed division planes but were then unable to complete division (Fig. 1d, Supplementary Video 1). Interestingly, some of the greatly enlarged Δ*cdpA* cells appeared to lyse suddenly but produced cell fragments that were sometimes capable of ongoing growth and division (Fig. 1d, arrows; Supplementary Video 1); in others, blebbing from cellular lobes was seen. These appear to be typical features of *H. volcanii* cell division mutants that are accompanied by ongoing chromosome replication and metabolism to maintain culture viability[10].

To verify the cell division phenotype attributed to *cdpA*, we reintroduced the *cdpA* gene under the control of the tryptophan-regulated promoter (*p.tna*) on a plasmid in the Δ*cdpA* background. This rescued the cell division defect in the presence of moderate (0.2 mM) or high (2 mM) concentrations of tryptophan (Trp) (Supplementary Fig. 2), confirming that the *cdpA* open reading frame (ORF) is responsible for the observed cell division phenotype. Overexpression of *cdpA* in a wild-type *H. volcanii* background caused no detected cell division or morphological changes (Supplementary Fig. 2a).

CdpA localizes at the mid-cell division ring but differs in sub-ring localization compared to FtsZ1 and FtsZ2

We investigated the subcellular localization of CdpA by expressing GFP-tagged CdpA from a plasmid in wild-type and Δ*cdpA* strain backgrounds. Fluorescence microscopy showed that CdpA-GFP in both strains localized as a band at mid-cell in almost all cells (Fig. 1e, Supplementary Fig. 3). With relatively high concentrations of Trp (2 mM), small extracellular fluorescent particles were also seen (Supplementary Fig. 3b), suggesting that excess CdpA-GFP promotes the generation of such particles from cells. CdpA-GFP fully complemented the cell division defect of the Δ*cdpA* strain in the presence of 0.2 mM Trp induction or greater, showing that the tagged protein is functional in division (Supplementary Fig. 3).

We then investigated the localization of CdpA together with FtsZ1 or FtsZ2 by production of pairs of fusion proteins from a plasmid in the wild-type background. The degree of co-localization observed

138 between CdpA-GFP and FtsZ1-mCherry was strong, with a correlation coefficient of > 0.7 in 79% of
139 cells (Fig. 2a). CdpA-GFP showed a somewhat higher background throughout the rest of the cell than
140 FtsZ1-mCherry, relative to the midcell bands (Fig. 2a, normalized intensity graphs). The co-production
141 of CdpA-GFP and FtsZ1-GFP did not cause a substantial change in cell shape and size, similar to when
142 FtsZ1-mCherry or FtsZ2-mCherry are moderately produced[10]. The co-production of CdpA-GFP and
143 FtsZ2-mCherry resulted in enlarged or filamentous cells (Fig. 2a), suggestive of a functional
144 interference between these two tagged proteins. Nevertheless, CdpA-GFP and FtsZ2-mCherry still
145 showed strong co-localization, with 84% of cells having a correlation coefficient of > 0.8 (Fig. 2a,
146 righthand panels). In many of these enlarged cells, CdpA-GFP and FtsZ2-mCherry were co-localized
147 around mid-cell, whereas in some cells they were found near the quarter positions of the long axis of
148 the cell (Fig. 2a).

149 To investigate protein localization at higher resolution within the division ring, Structured-Illumination
150 Microscopy (SIM) was used to visualize cells co-producing CdpA- and FtsZ- fusion proteins. Live cell
151 2D-SIM revealed that CdpA-GFP and FtsZ1/2-mCherry had differing localization patterns within the
152 mid-cell ring (Fig. 2b). Quantification of fluorescence intensities revealed that CdpA-GFP and FtsZ1- or
153 FtsZ2-mCherry foci were colocalized in some regions but were clearly separated in others (Fig. 2b);
154 similar results were seen with cells immobilised in vertical agarose micro-holes to view the cells end-
155 on using confocal microscopy (Supplementary Fig. 4). We then used 3D-SIM with the normal mounting
156 of cells on agarose pads, which further resolved the individual ring sub-structures, and we saw that
157 CdpA-GFP was highly discontinuous within the ring, appearing as distinct small foci with gaps in
158 fluorescence intensity between them (Fig. 2c). FtsZ1-GFP and FtsZ2-GFP rings appeared more
159 continuous but still showed substantial variations in structure and intensity around the ring (Fig. 2c,
160 Supplementary Fig. 5, Supplementary Video 2-4).

161 **CdpA has different effects on the localization of FtsZ1 and FtsZ2, and contributes strongly to their**
162 **coupling at mid-cell**

163 The division ring localization of CdpA, FtsZ1 and FtsZ2, and their different spatial patterns within the
164 ring, prompted us to investigate the dependency of CdpA and FtsZ1/FtsZ2 on each other for proper
165 assembly in the division ring. We assessed the localization of CdpA in the two *ftsZ* knockout strains
166 and vice versa. In the absence of FtsZ1, CdpA-GFP failed to localize as rings and infrequently appeared
167 as a faint midcell focus, and in an *ftsZ1/ftsZ2* double knock-out it showed a diffuse, non-localized signal
168 (Fig. 3a). On the other hand, FtsZ2 deletion did not prevent CdpA-GFP localization although it often
169 appeared as very irregularly structured, poorly condensed or indistinct rings (Fig. 3a). Thus, the proper
170 localization and midcell assembly of CdpA is strongly dependent on the presence of FtsZ1 and FtsZ2.

171 Deletion of *cdpA* had strikingly different effects on FtsZ1 and FtsZ2 function and localization patterns.
172 FtsZ1-mCh localizations in Δ*cdpA* appeared as rings but with broader zones compared to FtsZ1-mCh
173 ring structure in wild-type cells and occasional foci seen throughout the cells (Fig. 3b). Measurements
174 of the ratio of localized to non-localized FtsZ1-mCh per cell and each individual localization's thickness,
175 confirmed that the fluorescence in localized structures was similar in both strains, but the localizations
176 were relatively poorly condensed in many of the *ΔcdpA* cells compared to wild-type (Fig. 3b, graphs).
177 In these strains, the *cdpA* knockout resulted in ~30% of the total cells that we classified as filamentous
178 (cell area > 5 μm^2, circularity < 0.3) compared with ~5% in the wild-type (Supplementary Fig. 6). These
179 findings suggest that CdpA contributes to proper FtsZ1 ring condensation.

180 FtsZ2-GFP also showed poorly formed ring structures in the Δ*cdpA* background, but in contrast to
181 FtsZ1, localizations often appeared as foci, foci clusters, or short mispositioned filaments located along
182 the cell edge in a perpendicular orientation compared to normal rings (Fig. 3c). Consistent with a
183 previous observation[10], we saw that expression of FtsZ2-GFP caused a sensitive division defect,
184 resulting in somewhat enlarged cells in the wild-type and Δ*cdpA* backgrounds. Some cells showed
185 multiple localizations; the number of normal perpendicular orientated localizations of FtsZ2-GFP and

186 their frequency in relation to total cell length appeared to be reduced in Δ*cdpA* (Fig. 3c, graphs;
187 Supplementary Fig. 7).

188 Highly informative results were obtained when producing both FtsZ1-mCh and FtsZ2-GFP in the Δ*cdpA*
189 background. The absence of CdpA resulted in obvious uncoupling of FtsZ1 and FtsZ2 filaments, with a
190 wide range of correlation coefficients (0.3-1) in most cells (Fig. 3d). FtsZ1-mCh appeared as rings with
191 additional poorly condensed foci throughout the cells, whilst FtsZ2-GFP was seen as foci or
192 mispositioned filaments, as seen during the single expression experiments above (Fig. 3d). We further
193 examined these strains with a relatively low concentration of tryptophan induction (0.1 mM Trp),
194 reflecting lower expression level of FtsZ1-mCh and FtsZ2-GFP[10], and observed broader zones of FtsZ1-
195 mCh localization and foci or mispositioned FtsZ2-GFP, demonstrating strong uncoupling of the two
196 FtsZs (Supplementary Fig. 8). These data suggest that the uncoupling is not caused by the enlarged
197 cell sizes and expression levels of FtsZ-FP proteins. We conclude that CdpA plays an important role in
198 assembly of FtsZ1 and FtsZ2 at midcell by promoting FtsZ1 ring condensation and the correct
199 orientation and ring-coupling of FtsZ2 structures.

200 **CdpA is a relatively immobile midcell ring 'anchor' that has minimal effects on the dynamics of FtsZ1-**
201 **GFP and FtsZ2-GFP localization**

202 To investigate CdpA and FtsZ movement at midcell, and whether CdpA influences FtsZ dynamics within
203 the division ring, we monitored the fluorescence of CdpA-GFP and FtsZ1/2-GFP in live cells over time.
204 We initially recorded 3D-SIM images with 1 min intervals and saw that FtsZ1-GFP was dynamic within
205 the ring, with changes in the intensity and location of clusters of fluorescence intensity over time
206 (Supplementary Fig. 9, Supplementary Video 5), consistent with previous lower-resolution
207 observations[10]. In contrast, CdpA-GFP showed no such movement in the ring over the same period
208 (Supplementary Fig. 10, Supplementary Video 6).

209 To better enable cluster tracking and reduce bleaching during image acquisition, we used total internal
210 reflection fluorescence (TIRF) microscopy to record protein movement near the cell surface closest to
211 the coverslip. Visual inspection of kymographs generated from the TIRF data recorded at the division
212 ring using 4 s frame intervals over 15 min, suggested that clusters of FtsZ1-GFP fluorescence were
213 moving in a directional manner (Fig. 4a). Further analysis revealed that these clusters exhibited
214 complex zigzag and crossover patterns, reflecting FtsZ1-GFP cluster movement in both directions
215 around the division plane (Fig. 4a, Supplementary Video 7-8). FtsZ2-GFP showed similar zigzag-like
216 patterns, but they were generally slower than FtsZ1-GFP (imaging required 10 s intervals over 40 min,
217 Fig. 4b, Supplementary Fig. 11, Supplementary Video 9-10). In contrast, visualization of CdpA-GFP with
218 TIRF over the 15- and 40-min periods showed no substantial directional movement and greatly
219 reduced fluctuations of fluorescence intensity over time compared to the FtsZs (Fig. 4c, 4d,
220 Supplementary Fig. 11-12, Supplementary Video 11-14).

221 It is important to note that the function of FtsZ2-GFP in cell division is more severely affected by the
222 GFP tag than FtsZ1-GFP[10, 19], whereas CdpA-GFP is fully functional (Fig. 1f). The dynamics of FtsZ2-GFP
223 or its response to other proteins might therefore be significantly affected by the tag, compared to the
224 untagged native FtsZ2. Here, our aim instead was to determine whether the relative dynamics of each
225 of the existing FtsZ-GFPs is altered by the presence or absence of CdpA. In the absence of CdpA, FtsZ1-
226 GFP still showed clusters with apparently similar movement rates as the wild-type background, and as
227 expected, they often spanned a relatively uncondensed zone of localization around midcell (Fig. 4e,
228 Supplementary Video 15-17). We then measured the FtsZ1-GFP fluorescence intensity over time in a
229 square region near the centre of a localization, and this appeared to show irregular, non-periodic
230 fluctuations (Fig. 4f, Supplementary Fig. 13). To identify any periodicity or dominant frequencies, we
231 plotted the power spectrum density (PSD)[5] in 21 cells of each strain (Fig. 4g, Supplementary Fig. 14).
232 In the wild-type background, there was an elevated FtsZ1-GFP periodicity at ~0.003 Hz on average
233 compared to Δ*cdpA* in which the average fluctuations showed a simpler decay-like curve consistent

234 with a lack of periodicity detected within the 15 min. The wild-type signal around 0.003 Hz was
235 dominant in ~24% of cells, and weak or not evident in ~76%. This heterogeneity might reflect complex
236 patterns of polymerization within the ring, or cells at different stages of midcell maturation and
237 activity (Supplementary Fig. 14). In the absence of CdpA, FtsZ1 polymerization rates or types might be
238 affected, or the loss of ring structural integrity could also lead to the loss of the localized periodic
239 fluctuations.

240 With FtsZ2-GFP in Δ*cdpA*, we saw striking dynamic shifts in the cellular position and orientation of
241 FtsZ2-GFP localizations over time (Fig. 4h-i, Supplementary Video 18-23), consistent with the strong
242 uncoupling and mispositioning of FtsZ2-GFP in the static images (Fig. 3c). However, Like FtsZ1-GFP,
243 FtsZ2-GFP clusters clearly displayed movement consistent with dynamic polymerization within the
244 localized structures in Δ*cdpA* that was comparable to the wild-type background (Fig. 4h-i,
245 Supplementary Video 9-10, 18-23). We conclude that CdpA is relatively immobile within the ring but
246 strongly influences the stable assembly and positioning of the two FtsZ proteins at midcell whilst
247 having minimal or moderate influence on FtsZ-GFP dynamics within the localized structures.

248 **The three domains of CdpA have differing roles**

249 CdpA contains a strongly predicted N-terminal transmembrane domain (amino acids 17-149), a
250 cytoplasmic unstructured linker region (150-284) and a smaller C-terminal domain (285-328) (Fig. 1b,
251 5a). Together with the results above, this expected topology suggests a model in which CdpA tethers
252 and/or helps assemble and orientate cytoplasmic FtsZ filaments and potentially other components at
253 the midcell membrane. We further investigated this by assessing the contributions of the three main
254 regions to CdpA localization and function.

255 We initially found that an isolated N-terminal domain ($CdpA_{NTD}$-GFP) localized weakly at mid-cell, a
256 NTD deletion construct ($CdpA_{\Delta NTD}$-GFP) failed to localize, and a CTD deletion construct ($CdpA_{\Delta CTD}$-GFP)
257 efficiently localized at mid-cell (Fig. 5b). The $CdpA_{NTD}$ is therefore essential for midcell ring localization,
258 but insufficient without the $CdpA_{Linker}$ for the normal degree of localization. It is possible that the linker
259 contributes to interactions promoting CdpA's assembly into the ring, and/or it alleviates potential
260 steric interference by the GFP when attached directly to the $CdpA_{NTD}$.

261 To investigate the influence of the three CdpA domains on cell division and FtsZ localization, we
262 generated in-frame deletions (scar-less) of each of the three regions in the endogenous chromosomal
263 copy of *cdpA*. In the absence of the NTD ($cdpA_{\Delta NTD}$), the cells became filamentous (Fig. 5c,
264 Supplementary Fig. 15a); the $cdpA_{\Delta Linker}$ strain also showed a division defect of enlarged plate cells,
265 and $cdpA_{\Delta CTD}$ showed a heterogeneous mixture of enlarged plates and filamentous cells. Thus, division
266 defects were clear in all three strains, but they appear to have differing cell morphologies. However,
267 these shape differences were neutralized upon transformation with plasmids (containing various FtsZ-
268 FPs), which resulted in a greater frequency of highly filamentous cells (circularity < 0.2) and no
269 enlarged plates (Fig. 5c, Supplementary Fig. 15a). This is consistent with the known influence of *H.*
270 *volcanii* plasmids on cell shapes[19].

271 In all three CdpA domain deletion backgrounds, FtsZ1-mCh appeared as poorly condensed rings, broad
272 zones of patchy localization or complex helicoid structures, but this was accentuated with $cdpA_{\Delta Linker}$
273 (Fig. 5c, Supplementary Fig. 15b), suggesting that this deletion causes additional interference to FtsZ1
274 localization. Cells producing FtsZ2-GFP in all three backgrounds were filamentous, with infrequent
275 rings or localizations usually near one or both poles (Fig. 5c). The $cdpA_{\Delta Linker}$ background also caused
276 additional interference to FtsZ2-GFP localization because rings were rare or even not seen and foci
277 were often seen near the poles instead, whereas the $cdpA_{\Delta CTD}$ background gave the mildest FtsZ2-GFP
278 defect in which rings more frequent in than the other mutants but less than wild-type (Fig. 5c,
279 Supplementary Fig. 15c).

280 Interestingly, when we co-produced FtsZ1-mCh and FtsZ2-GFP in the various *cdpA* deletion strains (Fig.
281 5d, Supplementary Fig. 16), the patterns for each protein were similar but some appeared more
282 accentuated than the corresponding single-FtsZ-FP strains. In $cdpA_{\Delta NTD}$, FtsZ1-mCh localized as rings,
283 poorly condensed rings or foci, while FtsZ2-GFP formed patches, foci, or rare poor rings and they
284 showed a weaker correlation of localization than the wild-type (Fig. 5e). In $cdpA_{\Delta Linker}$, FtsZ1-mCh
285 showed striking irregular bands scattered along the length of the cells, and FtsZ2-GFP showed a
286 combination of diffuse signal with additional scattered foci (Fig. 5d). This strain showed the weakest
287 co-localization amongst the three *cdpA* domain deletions (Fig. 5e) and the FtsZ1-mCh localizations also
288 occupied a much greater area of the cells than the FtsZ2-GFP localizations (Fig. 5f). In $cdpA_{\Delta CTD}$, we saw
289 strongly co-localized rings of FtsZ1-mCh and FtsZ2-GFP, but these still appeared less frequently than
290 in the wild type and were often near one pole (Fig. 5d-f).

291 The combined results suggest that: 1) The N-terminal transmembrane domain and possibly the linker
292 region of CdpA are important for CdpA midcell localization, FtsZ1 ring condensation, and FtsZ2 ring
293 assembly and positioning; 2) The linker region of CdpA is necessary to prevent strong localization
294 defects caused by direct fusion of the NTD and CTD, possibly by preventing steric hindrance; 3) The C-
295 terminal domain of CdpA does not play a major role in the assembly and coupling of FtsZ1 and FtsZ2
296 rings, but has at least one other significant yet currently unknown role in cell division.

297 **CdpA is part of an anchor complex linked to FtsZ2 and other cell division proteins**

298 Given the above results, we searched for CdpA interactions with other *H. volcanii* proteins by isolating
299 affinity-tagged CdpA (CdpA-HA) from cross-linked *H. volcanii* cell lysates (in the Δ*cdpA* background)
300 using anti-HA magnetic beads. Bound proteins were eluted and analysed by western blots probed with
301 antibodies recognising HA, FtsZ1 and FtsZ2 (Fig. 6a). Both FtsZ1 and FtsZ2 were detected in the lysate
302 (L) and unbound (FT) samples, however, only FtsZ2 was clearly detected in the bound protein elution
303 (E) sample (Fig. 6a). Neither protein was detected in the elution from the control cells containing the
304 HA vector only (Fig. 6a). These results suggest that CdpA can exist in a complex with FtsZ2.

305 We carried out additional pull-down experiments with CdpA-HA and FtsZ2-HA in their corresponding
306 knock-out backgrounds, compared to the wildtype background with HA vector only as the control, and
307 we identified bound proteins by mass spectrometry (MS). FtsZ1 was detected in the bound-protein
308 elution of both the CdpA-HA and FtsZ2-HA pull-downs, albeit with only moderate statistical support,
309 as assessed by mean MS peak area quantification (Log_2 fold-change (FC)=2.7, p=0.10 for the CdpA-HA
310 pull-down, and Log_2FC=3.0, p=0.03 for the FtsZ2-HA pull-down, n=6 independent experiments each).
311 FtsZ2 was identified significantly in the CdpA-HA pulldown (Log_2FC=5.7, p=0.002), and as expected in
312 the FtsZ2-HA pull-down (Log_2FC=10.6, p=0.08). The FtsZ2-HA pull-down only identified one other
313 protein with statistical support (i.e., CetZ2, which was not detected in the HA controls; Supplementary
314 Table 3). The low detection rate in the FtsZ2-HA pull-downs might be due to the relatively low
315 expression of the FtsZ2-HA fusion (Supplementary Fig. 17) or interference by the HA tag (as seen with
316 the function of FtsZ2-GFP). However, the CdpA-HA construct was well expressed and complemented
317 the division defect of the Δ*cdpA* background used in the pull-downs (Supplementary Fig. 17). The
318 CdpA-HA pull-down MS data included other proteins previously implicated in cell division, including
319 SepF (HVO_0392, Log_2FC=4.3, p=0.01), CdpB1 (HVO_1691, Log_2FC=3.4, p=0.07) and CdpB2 (HVO_1964,
320 Log_2FC=3.1, p=0.02) (Supplementary Table 3). Other identified proteins recently linked to cell
321 envelope-related functions included actin-like protein volactin (HVO_2015, Log_2FC=2.5, p=0.06) and
322 small GTPase ArvA (OapA, HVO_3014, Log_2FC=2.8, p=0.04)[18, 20].

323 To predict how the cell division proteins interact with CdpA, we used Alphafold2 (AF2) Multimer with
324 two molecules each of CdpA, CdpB1, CdpB2, FtsZ2, and SepF, as preliminary AF2 runs and existing
325 homolog structures[13, 14] had indicated that each protein can dimerise or polymerise. This revealed a
326 strikingly coherent predicted structure, consistent with the current experimental results, that we refer
327 to as the anchor complex (Fig. 6b). Most of the visible interactions within the predicted anchor

complex are supported by low pairwise alignment error scores between the corresponding regions (Fig. 6c). The main exception to these relatively strong predictions was that the association between the anchor complex and FtsZ2 was quite weak, hinting that interactions between the anchor complex and FtsZ2 may occur via other unknown adaptors. The strongly predicted interactions notably include a direct association of the cytoplasmic short N-terminal helix of CdpA (residues 1-10) with the interface region of each CdpB1/2 heterodimer, which would bring CdpB1/2 close to the inner surface of the membrane (Fig. 6b, 6c). Furthermore, CdpA is predicted to participate in a ternary association with CdpB1 and SepF's N-terminal extension and membrane targeting sequence (MTS) that places the SepF MTS in an ideal position to penetrate the inner leaflet of the cytoplasmic membrane whilst also bound to CdpA at the interface of cytoplasm and membrane (Fig. 6b, 6c).

These experimental results and structural analysis have indicated that the CdpA NTD acts as a primary membrane anchor located at discrete positions around the division ring, where SepF is expected to play an adaptor-like role (braced by CdpB1/2 multimers) to connect the anchor complex with cytoplasmic ring components including FtsZ2. We found that CdpA has multiple functions, as the inter-domain disordered linker was critical for the proper condensation and positioning of FtsZ1 and FtsZ2 filaments, respectively, whereas the CTD was also important for division in other ways, likely through unknown interaction partners.

346 **Discussion**

347 In bacteria and eukaryotes, many proteins have been identified to contribute to division ring assembly
348 and anchoring. Here we identify and characterize the function of a ring assembly and anchor protein
349 in haloarchaea, which we named Cell division protein A (CdpA). We found clear roles for CdpA in
350 orchestrating the midcell assembly and co-positioning of FtsZ1 and FtsZ2 filaments to form the division
351 ring in the model archaeon *H. volcanii*. Several other proteins involved in archaeal dual-FtsZ division
352 have recently been identified, including SepF, CdpB1, and CdpB2[11, 13, 14], though their functions in the
353 haloarchaeal division mechanism are unclear. Based on the current findings, we developed a structural
354 model in which CdpA acts as the membrane-embedded component of a midcell anchor complex
355 (including SepF, CdpB1, and CdpB2 linked to the membrane though multiple direct interactions with
356 CdpA; Fig. 6). CdpA also functions as a tether and organizing center at relatively immobile and distinct
357 locations around the division ring to promote FtsZ1 and FtsZ2 ring formation and maintenance, and
358 likely other midcell ring proteins, via its cytoplasmic linker and C-terminal domains.

359 In bacteria, one of the best characterized FtsZ membrane linkage proteins is the widespread FtsA
360 actin-superfamily protein. The essentiality of FtsA varies among different species. For example, in
361 *Escherichia coli*, FtsA is essential[21], whereas in *Bacillus subtilis*, the *ftsA* gene can be deleted, although
362 this affects Z-ring formation and causes cells to become enlongated[22]. Here, we were able to delete
363 the *cdpA* gene in *H. volcanii*, which caused a division defect resulting in mixed populations of near-
364 normal and greatly enlarged cells. We directly observed some of the greatly enlarged cells forming
365 cellular fragments upon lysis of the main cell body, some of which were viable and capable of ongoing
366 growth and division. This likely explains the survival of many *H. volcanii* cell division mutant strains in
367 culture. As has been observed in bacteria, we anticipate that other currently uncharacterized
368 haloarchaeal proteins, and potentially CdpA-like proteins, are also involved in midcell ring assembly
369 or cytoskeletal protein anchoring. These may somewhat compensate for the loss of CdpA and enable
370 some of the cells to proliferate.

371 Super-resolution imaging revealed that CdpA forms a more discontinuous or patchy ring-like structure
372 at mid-cell compared to FtsZ1 or FtsZ2 rings and differing organization within the ring. FtsZ1 rarely
373 formed normal Z rings and instead formed broad and ill-defined—often helicoid—structures, that still
374 retained dynamic localization patterns. Although typical-looking FtsZ2-GFP rings were sometimes
375 observed in the absence of CdpA, FtsZ2-GFP foci or filaments frequently appeared strongly
376 mispositioned, including perpendicular to the normal ring along the cell edge. FtsZ2 also retained its
377 dynamic properties, resulting in frequent repositioning of the misplaced FtsZ2 foci and filaments. This
378 resulted in FtsZ1 and FtsZ2 becoming uncoupled in their subcellular localization patterns, supporting
379 the notion that they can polymerize independently of one another[10].

380 Our protein pull-down experiments detected CdpA in complex with FtsZ2 but not clearly with FtsZ1,
381 despite our finding that the proper localization of CdpA depends on the presence of both FtsZ2 and
382 especially FtsZ1 (and vice versa). Current observations would suggest that FtsZ1 associates only
383 indirectly with the CdpA-anchor complex, via another anchor, or in a manner that is not well
384 maintained during the pull-down assay procedure. The CdpA pull-downs also identified SepF and
385 CdpB1/2 amongst the interaction partners. The observed co-dependencies of localization, and the
386 similar poorly-condensed Z-ring structures observed in the absence of CdpA, SepF[11], or CdpB1/2[13, 14],
387 suggest a hypothesis in which these proteins assemble into a complex that functions in Z-ring assembly.

388 Previous studies reported that *H. volcanii* SepF is part of a complex with FtsZ2[11], and with CdpB1/2[13,
389 14]. Furthermore, SepF appears to localize at mid-cell via a short N-terminal amphipathic sequence,
390 which was expected to act as a membrane targeting sequence (MTS)[11]. The finding that the SepF MTS

391 alone was sufficient for midcell ring localization[11] suggests that this short sequence does more than
392 just potential membrane targeting. Our combined results and structural modelling (Fig. 6) support the
393 existence of a midcell anchor complex that forms through multiple intimate associations, including
394 the N-terminal extensions of CdpA and SepF interacting in different ways with CdpB1/2 heterodimers,
395 and SepF's MTS (at the very N-terminus) simultaneously associating with the CdpA NTD and partly
396 embedded in the cytoplasmic membrane. The SepF MTS may thereby be sufficient for midcell
397 localization[11] due to its likely association with CdpA. The main membrane anchoring component
398 appears to be the CdpA NTD, linked to and braced by multimers of SepF and CdpB1/2.

399 Consistent with the structural model (Fig. 6), our domain localization studies indicated that the CdpA
400 NTD is essential for its midcell localization, whereas the CTD was dispensable for midcell localization
401 but required for normal division. The NTD and linker regions appear to be critical for assembly and
402 anchoring of FtsZ1 and FtsZ2 rings, whereas the CTD seems to not strongly affect FtsZ1 and FtsZ2.
403 These observations suggest a multi-functional role of CdpA in *H. volcanii* division, where the long,
404 disordered linker and C-terminal domain also play important but currently undefined roles in tethering
405 or assembling other proteins at midcell.

406 CdpA shows some noteworthy similarities and differences to other division ring anchor proteins. In
407 bacteria, the FtsZ ring is typically anchored to the midcell membrane by FtsA, ZipA or SepF, whereas
408 in non-FtsZ archaeal division based on the ESCRT-III (CdvB) cytoskeletal proteins, CdvA is considered
409 to play a different anchor-like role. FtsA is broadly conserved in most bacteria and contains a short C-
410 terminal MTS and also directly interacts with FtsZ, recruiting it to the inner membrane[23, 24]. ZipA is an
411 integral inner membrane protein found in Gram-negative bacteria, and is comprised of a large C-
412 terminal globular cytoplasmic domain linked to a single N-terminal transmembrane domain via an
413 extended linker[25, 26]. FtsA and ZipA have overlapping functions but likely serve differing roles in
414 modulating division ring assembly[27, 28] Both FtsA and ZipA interact directly with FtsZ through an
415 interaction hub located at its C-terminal tail[29]. SepF is conserved in Gram-positive bacteria and
416 contains an N-terminal MTS and forms functional dimers, which interact with the C-terminal domain
417 of FtsZ[30, 31]. In the Crenarchaeota, *Sulfolobus* CdvA links ESCRT-III (CdvB) proteins to the cell membrane
418 via direct interactions and is thought to assemble on the membrane surface[32].

419 Compared to these proteins, CdpA exhibits highest topological similarity to ZipA, suggesting an
420 analogous midcell anchor role. However, ZipA-GFP in *E. coli* showed clear movement around the
421 division ring[33], yet we found that CdpA-GFP remains relatively stable at mid-cell in *H. volcanii*,
422 suggesting they may operate via differing mechanisms within the ring. SepF homologues from
423 different bacterial species can polymerize into large protein rings associated with cell wall
424 remodelling[34], whereas there is no evidence to show that archaeal SepF is capable of polymerization[11,
425 12]. Our discovery of an archaeal FtsZ-assembly and transmembrane anchor protein confirms this as a
426 feature important in both major branches of microbial life.

427

428 **Methods**

429 **Identification, phylogeny, and structural analysis of CdpA and CdpA-like sequences**

430 The reference amino acid sequence of HVO_0739 (CdpA) was first input into JackHMMER[35] to search
431 against UniProtKB database[36] with three iterations restricted by taxonomy in Archaea (taxid:2157).
432 The output HMM profile was used to scan the amino-acid sequences of all proteins in 1,587 high
433 quality diverse archaeal genomes from NCBI RefSeq database[37] with a significance threshold of an E-
434 value of 10^{-5}. The identified sequences were then confirmed using a BLASTP v2.13.0[38] search against
435 the reference CdpA sequence with an E-value cut-off of 10^{-5}; sequences giving no hit in the BLASTP
436 search result were removed. The remaining 1,336 sequences were taken as CdpA candidates. Of these,
437 proteins with a length between 80% to 120% of HVO_0739 (i.e., 260-400 residues) and with four
438 transmembrane segments (predicted using TMHMM v2.0)[39] within the N-terminal 75% of the
439 sequences were taken as CdpA family proteins (470 sequences), and the remaining 866 were
440 designated CdpA-like proteins.

441 Multiple alignment of the 470 CdpA sequences was then performed using MUSCLE v3.8.31[40]. A
442 neighbour-joining tree based on the amino-acid alignment was constructed using PHYLIP v3.698[41] with
443 the default model and 1,000 bootstrap replicates. HVO_2016 (*H. volcanii* CdpA-like protein) was
444 included as the outgroup to root the tree. The alignment was then reordered by tree structure. A
445 reduced version of the alignment was generated by removing columns that had a gap in the *H. volcanii*
446 CdpA reference sequence. This alignment was displayed using UGENE v46.0[42]. Taxonomy annotation
447 was based on the NCBI Taxonomy database. PsiPred v4.02[43] was used to estimate the secondary
448 structure of CdpA along the alignment.

449 Protein 3D structure predictions were downloaded in monomer form from the Alphafold structure
450 database (https://www.alphafold.ebi.ac.uk) or generated as complexes using Alphafold v2.3.1
451 (Multimer)[44] using default settings with the full BFD reference database. Structures were visualised
452 and rendered with PyMOL[45] v2.5.1. Transmembrane topology (Fig. 1b, 6b) was predicted with
453 Phobius[46].

454 **Growth of *H. volcanii* strains**

455 The *H. volcanii* cultures were grown in Hv-Cab medium[9, 47]. Where necessary as auxotrophic
456 requirements, media were supplemented with uracil (50 µg/mL) for Δ*pyrE2* strains. To control gene
457 expression via the *p.tnaA* promoter, the indicated concentration of L-tryptophan (Sigma–Aldrich) was
458 supplemented in these cultures. For microscopic imaging, the cultures were incubated at 42°C with
459 rotary shaking (200 rpm) and were maintained in log growth ($OD_{600} < 0.8$) for at least 2 days before
460 sampling for analysis of mid-log cultures. Representative data displayed in this paper are
461 representative of at least two independent biological replicate experiments.

462 **Construction of plasmids for gene deletion and genomic modification in *H. volcanii***

463 The plasmids, oligonucleotide sequences, and strains are given in the Supplementary Tables 1 and 2.
464 The plasmid pTA131 was used as the basis to construct the plasmids for gene deletion[48]. To make the
465 plasmid for *cdpA* deletion, the upstream and downstream flanks for homologous recombination on
466 either side of *cdpA* were PCR amplified from *H. volcanii* H26 genomic DNA, using the primers given in
467 Supplementary Table 1. The upstream flank fragment and downstream fragments were digested with
468 HindIII and BamHI, respectively, and cloned into pTA131 (at HindIII-BamHI) using Gibson assembly
469 reagents (NEB), resulting in pTA131_up_down_0739. The plasmids pTA131_CdpA_delNTD for N-
470 terminal domain (17-149 aa) deletion and pTA131_CdpA_delLinker for linker region deletion (150-284
471 aa) were obtained synthesised and cloned (Genscript). To make the plasmid pTA131_CdpA_delCTD
472 for C-terminal domain (285-328 aa) deletion, the upstream flank and downstream flanking fragments
473 of the CdpA C-terminal domain were amplified by using the primers in Supplementary Table 1 and
474 cloned into pTA131 (at HindIII-BamHI) using Gibson assembly (NEB) as described above.

475 Demethylated plasmids pTA131_up_down_0739, pTA131_CdpA_delNTD, pTA131_CdpA_delLinker,
476 and pTA131_CdpA_delCTD were used to transform *H. volcanni* H26 separately by using the pop-in-
477 pop-out method as described previously to delete the corresponding gene fragments[48]. Allele-
478 specific PCR was used to verify the expected deletion chromosomal structure, resulting in H26-base
479 strains carrying the *cdpA* mutations: Δ*cdpA*, $cdpA_{\Delta NTD}$, $cdpA_{\Delta Linker}$, and $cdpA_{\Delta CTD}$ (Supplementary Table
480 2).

481 **Construction of plasmids for gene expression in *H. volcanii***

482 The plasmids pTA962[49] or pIDJL40[9] (containing GFP) were used as the basis to construct plasmids for
483 controlled expression of the *cdpA* genes or modified versions. To construct pTA962-*cdpA*, the *cdpA*
484 ORF (HVO_0739) was amplified from *H. volcanii* H26 genomic DNA using primers HVO_0739_r and
485 HVO_0739_r, then the product was cloned between the NdeI and BamHI sites of pTA962. The *cdpA*
486 ORF was also amplified without its stop codon, then cloned between the NdeI and BamHI sites of
487 pIDJL40, to create the *cdpA*-gfp fusion. For dual expression of *cdpA*-gfp and *ftsZ1/2*-mCherry, PvuII
488 fragment of pTA962-*ftsZ1*-mCherry or *ftsZ2*-mCherry[10] (containing a *p.tnaA-ftsZ*-mCherry gene fusion)
489 were ligated into HindIII-cut (Klenow blunt-ended) pIDJL40_HVO_0739 containing (*cdpA*-GFP),
490 creating plasmid with two independent copies of the CdpA-GFP and FtsZ1/2-mCherry.

491 To construct the $CdpA_{NTD}$-GFP fusion, the N-terminal domain of CdpA (1-149 aa) was amplified from
492 *H. volcanii* H26 genomic DNA using primers HVO_0739_f and CdpA_NTD_R, then the product was
493 cloned between NdeI and BamHI sites of pIDJL40. The mutant CdpA without the C-terminal domain
494 and without the N-terminal sequences were amplified from *H. volcanii* H26 and mutant $cdpA_{\Delta NTD}$
495 genomic DNA, respectively, by using the primers in Supplementary Table 1, and then cloned between
496 NdeI and BamHI sites of pIDJL40, to create $CdpA_{\Delta CTD}$-GFP and $CdpA_{\Delta NTD}$-GFP fusions. To construct
497 pHVID1-HA, synthetic DNA fragments encoding the HA tag with EcoRI and NotI overhangs were
498 obtained from Integrated DNA Technologies (IDT). These fragments were subsequently cloned into
499 the pHVID1 vector. To generate CdpA and FtsZ2 HA tagged plasmids, the respective genes amplified
500 from pIDJL40_*cdpA* and pIDJL40- *ftsZ2* were cloned between NdeI and BamHI sites of pHVID1-HA
501 plasmid, respectively. All plasmids were demethylated by passage through *E. coli* C2925 and re-
502 purified before transfer to *H. volcanii* H26 by polyethylene glycol-mediated spheroplast
503 transformation[48].

504 **Microscopy**

505 *Phase-contrast and epifluorescence microscopy:* a 2 µl sample of mid-log culture was loaded on a 1%
506 agarose pad containing 18% buffered saltwater (BSW) on a glass slide at room temperature, and a
507 #1.5 glass coverslip was placed on top[10]. The images were acquired on a GE DeltaVision Elite
508 microscope with a pco.edge 5.5 sCMOS camara and an Olympus 100X Plan Apo/NA 1.4 objective using
509 a FITC filter (ex 464-492 nm: em 500-549 nm) and mCherry filter set (ex 557-590, em 598-617 nm) for
510 visualizing GFP-tagged and mCherry-tagged proteins, respectively.

511 *Time-lapse microscopy:* the sample was prepared by using submerged sandwich technique as
512 previously described[10]. A 2 µl sample of mid-log culture was placed on a 0.3% wt/vol agarose pad
513 (containing the medium for the growth) prepared on an 8-mm glass-based (#1.5) FluoroDish (WPI). A
514 4 mL volume of medium was added to the FluoroDish to cover the agarose pad, and the lid was placed
515 on the FluoroDish to avoid evaporation. The images were captured at 42°C every 10 mins for 24 hrs
516 on a Nikon TiE2 inverted Fluorescence deconvolution microscope fitted with a 100 X oil-immersion
517 phase-contrast NA 1.45 objective.

518 *2D- and 3D-Structured Illumination Microscopy (SIM):* Samples were prepared on agarose pads as
519 described above for phase-contrast and epifluorescence microscopy. Images were captured on a Delta
520 Vision OMX SR 3D Structured Illumination Microscope with a 60 X Plan 1.42 NA Oil Immersion
521 Objective at room temperature for visualizing fluorescent fusion proteins, or at 42°C for 3D-SIM time-

522 lapse imaging. GFP and mCherry signals were collected through a FITC and a TRITC filter, respectively.
523 3D-SIM images were sectioned using a 125 nm z-step. The reconstructed images-stacks were 3D
524 rendered and visualized by using IMARIS x64 9.6.0 (Bitplane Scientific). 3D-SIM time series (acquired
525 every 30s – 2 min as required) were compiled from single time points using Imaris to create a time-
526 lapse series, followed by bleach correction (Histogram Match) and registration (using 'translation' in
527 TurboReg) in Image J 1.53v. The 3D intensity plots were generated by using '3D surface plot" in Image
528 J 1.53 v. Two regions of interest were monitored overtime show how FtsZ- or CdpA-GFP fluorescence
529 fluctuates in the Z ring.

530 *Confocal imaging for standing cells:* Production of microholes in agarose pads for standing cell
531 trapping were performed as previously described for bacterial cells[4, 50], with some required
532 modification for imaging archaeal cells. Liquefied agarose (4% w/v) in Hv-Cab media was dispersed on
533 glass slides and the silica mold was placed on top. Once the agarose solidified, the mold was removed
534 and ~ 4 µl of live cell mid-log culture was loaded on the top followed by placing the glass slides on a
535 microcentrifuge for a brief centrifuging to trap the cells in a vertical position in micron-sized holes in
536 agarose pads. The excess liquid was then removed, and the agarose pad was covered with a pre-
537 cleaned #1.5 cover glass. The confocal images of cells expressing CdpA-GFP and FtsZ-mCherry were
538 acquired on Leica STELLARIS SP8 confocal microscope equipped with a 63X oil immersion objective.
539 The Lightning module was used to generate deconvolved images.

540 *Total Internal Reflection fluorescence (TIRF) microscopy:* Samples were prepared as described for time-
541 lapse microscopy. The TIRF imaging was performed using a Nikon TiE-2 N-STORM microscope
542 operated in TIRF mode on a stage top incubator (OKO-lab) set to 42°C, equipped with a 100 X 1.49 NA
543 TIRF objective. The TIRF angle was set optimize the signal to noise ratio at a fixed angle of ~100°. The
544 imaging settings were chosen to minimize photobleaching with the power intensity setting as 5% and
545 the exposure time as ~ 150 – 200 ms. The dynamics of FtsZ1-GFP proteins were imaged at 4 second
546 intervals for 15 mins, and FtsZ2-GFP were imaged at 10 second intervals for 40 min. CdpA-GFP were
547 imaged either at 4 second intervals for 15 mins or 10 second intervals for 40 mins.

548 **Image analysis**

549 The analysis for cell shape (area vs circularity), FtsZ1/2 and CdpA medial localization along the cell long
550 axis, and FtsZ1-mCh intensity ratio and localization thickness were performed as described
551 previously[10]. The number of correct positioned FtsZ2-GFP rings per cell was manually counted and
552 plotted against cell length determined by FIJI.

553 For the dynamic analysis from TIRF data[5], fluorescence images were stabilized, and registered
554 (StackReg, Translation), and corrected for photobleaching (simple ratio), interpolated to 20 nm/pixel
555 via the bicubic method in Image J, and moving averaged over a 12-frame window of time. The
556 fluorescence intensity of an FtsZ polymer along the direction of its movement in each frame was
557 determined from the intensity along a line with a width of 25 interpolated pixels (~ 500 nm) manually
558 drawn across the full length of the path of the FtsZ polymer. This line was then used to plot the
559 kymograph (line width = 25) then background subtraction rolling ball =25, and smooth (for display
560 purpose). The speeds of clusters were calculated by manually measuring the slopes of leading and
561 trailing edges of clear fluorescence zigzags in the kymograph. The distributions of speed of FtsZ-FP
562 clusters were plotted in OrginPro (2021). For analysis of Z-ring intensity fluctuations during TIRF time-
563 lapse imaging, briefly, a cell of interest was cropped out from both fluorescence and bright-field
564 images. Second, the cell was rotated to align the Z-ring horizontally. Fluorescence background within
565 the cell was calculated by averaging the total integrated intensity over the area defined by the cell
566 contour. A square region of interest (ROI) with 3×3 pixels in the center of the ring was then chosen
567 manually. The corrected intensity was calculated as the integrated intensity within the ROI after
568 background subtraction and smoothed by a moving-average filter with a window size of 5 time points
569 in OriginPro (2021).

570
571 The Power Spectral Density (PSD) analysis was conducted using custom Matlab scripts. Firstly, a cell
572 of interest was cropped out from both fluorescence and bright-field images. The fluorescence images
573 were then registered to the bright-field image and corrected for sample/stage drift and
574 photobleaching. Following this, the cell was rotated manually to align the Z-ring horizontally. To
575 determine fluorescence background within the cell, the total integrated intensity over the area
576 defined by the cell outline was averaged. A square region of interest (ROI) with 3×3 pixels at the center
577 of the ring was then chosen manually. The local FtsZ-GFP (I) was computed as the integrated intensity
578 within the ROI after background subtraction.

579 Using fluorescence intensity time trace, $I(t)$, from the center of the division ring, the PSD curves were
580 calculated. This involved subtracting the mean value $\langle I(t)\rangle$ from $I(t)$ and subsequently applying the
581 Fast-Fourier Transform (FFT) to the shifted time trace (fft function in Matlab). For each cell, the PSD
582 curve across different frequencies f was then calculated as follows:

583 $$PSD(f) = \frac{|FFT(I(t) - \langle I(t)\rangle)|}{n\Delta f \cdot Var(I(t))},$$

584 where n is the total number of frames of the trace and Δf is the frame rate ($1/4\ s^{-1}$). Note that the
585 PSD was normalized by the squared magnitude of the intensity trace (variance of $I(t)$). The mean PSD
586 curves were generated by averaging the PSD curves of individual cells in each strain.

587 The FtsZ1/FtsZ2 localization patterns were analyzed in Matlab 2019b (MathWorks). The phase-
588 contrast images were first preprocessed using a bottom-hat transform (imbothat function) with a disk-
589 shaped structuring element of a radius of 30 pixels for the kernel. These were binarized and individual
590 cells were segmented (bwconncomp function). Cell debris were excluded by removing objects with
591 area less than 1 μm^2 (~237 pixels). The filtered cell outline was parametrically smoothed by fitting
592 each component of cell outline (i.e. x- and y-components in the Cartesian coordinate system) with two
593 Fourier expansions up to the 8th order mode.

594 To quantify the localization patterns of FtsZ1 and FtsZ2, fluorescent images were pre-treated by
595 subtracting the average intensity of the background (calculated from the fluorescence images,
596 excluding regions of the detected cells). Additionally, a top-hat transform (imtophat function) was
597 applied with a disk-shaped structuring element of a radius of 10 pixels. FtsZ1 and FtsZ2 clusters within
598 each cell were identified and segmented by converting the processed fluorescence images to 8-bit
599 and applying the extended-maxima transform (imextendedmax function) with a threshold value of 1.
600 Small fluctuations in FtsZ1 and FtsZ2 fluorescence signals were neglected by removing clusters less
601 than 4 pixels. The localization area of FtsZ1/FtsZ2 in each cell is then defined as the total area of all
602 FtsZ1/FtsZ2 clusters found within the cell outline. The ratio of FtsZ2 localization area to FtsZ1
603 localization area was then determined for each cell. Cells were excluded from the analysis if either
604 FtsZ1 or FtsZ2 clusters were undetectable within the cell or if the cell exhibited a signal-to-noise ratio
605 of less than 2.

606 **Immunoprecipitation of HA-tagged CdpA**

607 The method was employed as describe by previous work[11] but with modifications. H26-HA and CdpA-
608 HA strains were grown in 300 mL of Hv-cab medium supplemented with 2 mM Trp until their OD_{600}
609 reached 0.5. The cells were harvested by centrifugation at 6,000 x g for 15 min. The pelleted cells were
610 resuspended in 30 mL of 18% buffered salt water supplemented with 10 mM HEPES. For crosslinking
611 1.5% (w/v) formaldehyde was added to the cell suspension, and the mixture was incubated at room
612 temperature for 10 min with constant shaking. The crosslinking reaction was stopped by adding 20 mL

613 of 18% buffered salt-water containing 1.25 M glycine. The cells were centrifuged again for 15 min at
614 6,000 x g. The cell pellet was washed twice with 18% buffered salt water with 1.25 M glycine. After
615 the final wash, the cell pellet was resuspended in 3 mL of lysis buffer (1X PBS, 10 mM MgCl2, 10 µg/ml
616 DNase I and protease inhibitor cocktail). The cells where lysed by sonication for 5 min, with 5 sec on
617 and 5 sec off cycle at 35% amplitude. To remove the cell debris lysed cells were centrifuged at 8,000
618 rpm for 15 min at 4 °C in a microcentrifuge. The supernatant was used for immunoprecipitation with
619 washed anti-HA magnetic beads (Thermo Scientific) as described in the manufacturer's instructions.
620 The supernatant (1 mL) was added to 0.5 mg of anti-HA beads and incubated at room temperature for
621 30 min with gentle mixing. The beads were washed twice with buffer (Tis–buffered saline with 0.05%
622 Tween –20 Detergent) and eluted with 0.1 M glycine pH 2.0.

623 **Western blotting**

624 Samples were first run on a sodium dodecyl-sulphate polyacrylamide gel electrophoresis (SDS-PAGE)
625 and then electro transferred to a nitrocellulose membrane using the BioRad trans-blot turbo transfer
626 system. The membrane was blocked overnight in 5% (w/v) skim milk in Tris-buffered saline with 0.05%
627 Tween-20 (TBST). A primary antibody recognizing heamagglutanin (HA) (Thermo Fisher Scientific, Cat#
628 26183) (1:10,000), FtsZ1[10] (1:1,000) and FtsZ2[10] (1:2,000) were incubated with membrane for 2 h with
629 constant shaking at RT. Following that the membrane was incubated with the secondary antibody
630 against mouse (Goat anti-mouse IgG-HRP; AbCam 6789) for 1 h in a 1:5,000 dilution. Bands were
631 detected with enhanced chemiluminescence reagents (Thermo-Fisher) using an Amersham Imager
632 600 system.

633 **Mass spectrometry (MS)**

634 Fifty microgram of eluted proteins from the pull-down assay were subjected to trypsin digestion using
635 Promega Trypsin Gold, mass spectrometer grade (1 µg/µL) in 50 mM acetic acid. The digested samples
636 were processed for clean-up using solid-phase extraction (SPE). An equivalent amount of protein (15
637 µg) for each sample was loaded onto the SPE columns, which were then washed, and peptides eluted.
638 Columns were manually prepared using Empore SDS-RPS (Styrenedivinylbenzene reverse phase
639 sulfonate) with a pipette tip. The SDB-RPS based tips were used for peptide clean up.

640 Eluted samples were dried in a vacuum centrifuge, and peptides were reconstituted in the injection
641 solvent suitable for the LC/MS system. Analysis was performed on a Q Exactive Plus mass
642 spectrometer (Thermo Fisher Scientific), and the MS/MS data files were analyzed using PEAKS Studio
643 against *Haloferax volcanii* predicted proteome database using Uniprot. The MS peak areas obtained
644 for the peptides were then used for statistical analyses.

645

646 **References**

647 1. Adams, D.W. & Errington, J. Bacterial cell division: assembly, maintenance and disassembly of
648 the Z ring. *Nature Reviews Microbiology* **7**, 642-653 (2009).
649 2. Osawa, M. & Erickson, H.P. Liposome division by a simple bacterial division machinery.
650 *Proceedings of the National Academy of Sciences* **110**, 11000-11004 (2013).
651 3. Szwedziak, P., Wang, Q., Bharat, T.A., Tsim, M. & Löwe, J. Architecture of the ring formed by
652 the tubulin homologue FtsZ in bacterial cell division. *Elife* **3**, e04601 (2014).
653 4. Bisson-Filho, A.W. et al. Treadmilling by FtsZ filaments drives peptidoglycan synthesis and
654 bacterial cell division. *Science* **355**, 739-743 (2017).
655 5. Yang, X. et al. GTPase activity–coupled treadmilling of the bacterial tubulin FtsZ organizes
656 septal cell wall synthesis. *Science* **355**, 744-747 (2017).
657 6. Aylett, C.H. & Duggin, I.G. The tubulin superfamily in archaea. *Prokaryotic Cytoskeletons:*
658 *Filamentous Protein Polymers Active in the Cytoplasm of Bacterial and Archaeal Cells*, 393-417
659 (2017).
660 7. Liao, Y., Ithurbide, S., de Silva, R.T., Erdmann, S. & Duggin, I.G. Archaeal cell biology: diverse
661 functions of tubulin-like cytoskeletal proteins at the cell envelope. *Emerging Topics in Life*
662 *Sciences* **2**, 547-559 (2018).
663 8. Vaughan, S., Wickstead, B., Gull, K. & Addinall, S.G. Molecular evolution of FtsZ protein
664 sequences encoded within the genomes of archaea, bacteria, and eukaryota. *Journal of*
665 *molecular evolution* **58**, 19-29 (2004).
666 9. Duggin, I.G. et al. CetZ tubulin-like proteins control archaeal cell shape. *Nature* **519**, 362-365
667 (2015).
668 10. Liao, Y., Ithurbide, S., Evenhuis, C., Löwe, J. & Duggin, I.G. Cell division in the archaeon
669 Haloferax volcanii relies on two FtsZ proteins with distinct functions in division ring assembly
670 and constriction. *Nature microbiology* **6**, 594-605 (2021).
671 11. Nussbaum, P., Gerstner, M., Dingethal, M., Erb, C. & Albers, S.V. The archaeal protein SepF is
672 essential for cell division in Haloferax volcanii. *Nat Commun* **12**, 3469 (2021).
673 12. Pende, N. et al. SepF is the FtsZ anchor in archaea, with features of an ancestral cell division
674 system. *Nature Communications* **12**, 3214 (2021).
675 13. Nussbaum, P. et al. Proteins containing photosynthetic reaction centre domains modulate
676 FtsZ-based archaeal cell division. *Nat Microbiol* **9**, 698-711 (2024).
677 14. Zhao, S. et al. Widespread photosynthesis reaction centre barrel proteins are necessary for
678 haloarchaeal cell division. *Nat Microbiol* **9**, 712-726 (2024).
679 15. Darnell, C.L. et al. The ribbon-helix-helix domain protein CdrS regulates the tubulin homolog
680 ftsZ2 to control cell division in archaea. *MBio* **11**, 10.1128/mbio. 01007-01020 (2020).
681 16. Liao, Y. et al. CdrS is a global transcriptional regulator influencing cell division in Haloferax
682 volcanii. *Mbio* **12**, 10.1128/mbio. 01416-01421 (2021).
683 17. Braun, F. et al. Cyclic nucleotides in archaea: Cyclic di-AMP in the archaeon Haloferax volcanii
684 and its putative role. *Microbiologyopen* **8**, e00829 (2019).
685 18. Schiller, H. et al. Identification of structural and regulatory cell-shape determinants in
686 Haloferax volcanii. *Nat Commun* **15**, 1414 (2024).
687 19. Ithurbide, S., de Silva, R.T., Brown, H.J., Shinde, V. & Duggin, I.G. A vector system for single
688 and tandem expression of cloned genes and multi-colour fluorescent tagging in Haloferax
689 volcanii. *Microbiology (Reading)* **170** (2024).
690 20. Mills, J. et al. Extracellular vesicle formation in Euryarchaeota is driven by a small GTPase. *Proc*
691 *Natl Acad Sci U S A* **121**, e2311321121 (2024).
692 21. Addinall, S.G. & Lutkenhaus, J. FtsA is localized to the septum in an FtsZ-dependent manner.
693 *Journal of bacteriology* **178**, 7167-7172 (1996).
694 22. Beall, B. & Lutkenhaus, J. Impaired cell division and sporulation of a Bacillus subtilis strain with
695 the ftsA gene deleted. *Journal of bacteriology* **174**, 2398-2403 (1992).

23. Pichoff, S. & Lutkenhaus, J. Tethering the Z ring to the membrane through a conserved membrane targeting sequence in FtsA. *Molecular microbiology* **55**, 1722-1734 (2005).
24. Pichoff, S. & Lutkenhaus, J. Identification of a region of FtsA required for interaction with FtsZ. *Molecular microbiology* **64**, 1129-1138 (2007).
25. Mosyak, L. et al. The bacterial cell-division protein ZipA and its interaction with an FtsZ fragment revealed by X-ray crystallography. *The EMBO journal* **19**, 3179-3191 (2000).
26. Moy, F.J., Glasfeld, E., Mosyak, L. & Powers, R. Solution structure of ZipA, a crucial component of Escherichia coli cell division. *Biochemistry* **39**, 9146-9156 (2000).
27. Cameron, T.A., Vega, D.E., Yu, C., Xiao, H. & Margolin, W. ZipA uses a two-pronged FtsZ-binding mechanism necessary for cell division. *Mbio* **12**, e02529-02521 (2021).
28. Pichoff, S. & Lutkenhaus, J. Unique and overlapping roles for ZipA and FtsA in septal ring assembly in Escherichia coli. *The EMBO journal* (2002).
29. Ortiz, C., Natale, P., Cueto, L. & Vicente, M. The keepers of the ring: regulators of FtsZ assembly. *FEMS microbiology reviews* **40**, 57-67 (2016).
30. Hamoen, L.W., Meile, J.C., De Jong, W., Noirot, P. & Errington, J. SepF, a novel FtsZ-interacting protein required for a late step in cell division. *Molecular microbiology* **59**, 989-999 (2006).
31. Sogues, A. et al. Essential dynamic interdependence of FtsZ and SepF for Z-ring and septum formation in Corynebacterium glutamicum. *Nature communications* **11**, 1641 (2020).
32. Samson, R.Y. et al. Molecular and structural basis of ESCRT-III recruitment to membranes during archaeal cell division. *Mol Cell* **41**, 186-196 (2011).
33. Söderström, B., Chan, H., Shilling, P.J., Skoglund, U. & Daley, D.O. Spatial separation of FtsZ and FtsN during cell division. *Molecular microbiology* **107**, 387-401 (2018).
34. Wenzel, M. et al. Control of septum thickness by the curvature of SepF polymers. *Proceedings of the National Academy of Sciences* **118**, e2002635118 (2021).
35. Johnson, L.S., Eddy, S.R. & Portugaly, E. Hidden Markov model speed heuristic and iterative HMM search procedure. *BMC bioinformatics* **11**, 1-8 (2010).
36. Coudert, E. et al. Annotation of biologically relevant ligands in UniProtKB using ChEBI. *Bioinformatics* **39**, btac793 (2023).
37. O'Leary, N.A. et al. Reference sequence (RefSeq) database at NCBI: current status, taxonomic expansion, and functional annotation. *Nucleic acids research* **44**, D733-D745 (2016).
38. Camacho, C. et al. BLAST+: architecture and applications. *BMC bioinformatics* **10**, 1-9 (2009).
39. Krogh, A., Larsson, B., Von Heijne, G. & Sonnhammer, E.L. Predicting transmembrane protein topology with a hidden Markov model: application to complete genomes. *Journal of molecular biology* **305**, 567-580 (2001).
40. Edgar, R.C. MUSCLE: multiple sequence alignment with high accuracy and high throughput. *Nucleic acids research* **32**, 1792-1797 (2004).
41. Felsenstein, J. PHYLIP (phylogeny inference package), version 3.5 c. (Joseph Felsenstein., 1993).
42. Okonechnikov, K., Golosova, O., Fursov, M. & Team, U. Unipro UGENE: a unified bioinformatics toolkit. *Bioinformatics* **28**, 1166-1167 (2012).
43. Buchan, D.W. & Jones, D.T. The PSIPRED protein analysis workbench: 20 years on. *Nucleic acids research* **47**, W402-W407 (2019).
44. Jumper, J. et al. Highly accurate protein structure prediction with AlphaFold. *nature* **596**, 583-589 (2021).
45. Schrodinger, L. The PyMOL molecular graphics system. *Version* **1**, 8 (2015).
46. Kall, L., Krogh, A. & Sonnhammer, E.L. Advantages of combined transmembrane topology and signal peptide prediction--the Phobius web server. *Nucleic Acids Res* **35**, W429-432 (2007).
47. de Silva, R.T. et al. Improved growth and morphological plasticity of Haloferax volcanii. *Microbiology (Reading)* **167** (2021).
48. Allers, T., Ngo, H.-P., Mevarech, M. & Lloyd, R.G. Development of additional selectable markers for the halophilic archaeon Haloferax volcanii based on the leuB and trpA genes. *Applied and environmental microbiology* **70**, 943-953 (2004).

747 49. Allers, T., Barak, S., Liddell, S., Wardell, K. & Mevarech, M. Improved strains and plasmid
748 vectors for conditional overexpression of His-tagged proteins in Haloferax volcanii. *Applied*
749 *and environmental microbiology* **76**, 1759-1769 (2010).
750 50. Söderström, B., Badrutdinov, A., Chan, H. & Skoglund, U. Cell shape-independent FtsZ
751 dynamics in synthetically remodeled bacterial cells. *Nature Communications* **9**, 4323 (2018).

752

753 **Acknowledgments**

754 This study was supported by the University of Technology Sydney Chancellor's Research Fellowship
755 (PR021-13161 to Y.L.) and by the Australian Research Council (FT160100010 to I.G.D, and
756 DP220101143 to B.S.). For technical and facilities management support, we thank Matt Padula from
757 the Proteomics Core Facility, UTS, and Amy Bottomley, Christian Evenhuis and Louise Cole from the
758 Microbial Imaging Facility, UTS.

759 **Author Contributions**

760 Y.L and I.G.D. designed the research. Y.L. constructed most of the plasmids, strains and conducted the
761 primary microscopy imaging and analyses. V.D.S constructed plasmids and strains for pull-down
762 experiments and performed immunoprecipitation, western blot and mass-spectrometry analyses. D.H
763 performed phylogeny analysis of CdpA and CdpA-like sequences and contributed the production of
764 some image analysis figures using R programming. Z.X. performed PSD analysis and quantified the
765 localization area of FtsZ1/FtsZ2 in Matlab. B.S. contributed to the TIRF imaging and confocal imaging
766 of standing cells. K.A.M, and I.G.D. performed Alphafold2 Multimer prediction and analysis. Y.L. and
767 I.G.D. interpreted results and wrote the original draft. All authors reviewed and gave scientific input
768 to revise the manuscript. Y.L and I.G.D managed and supervised the project and acquired funding.

769 **Competing interests statement**

770 The authors declare no competing interests.

771

Figures

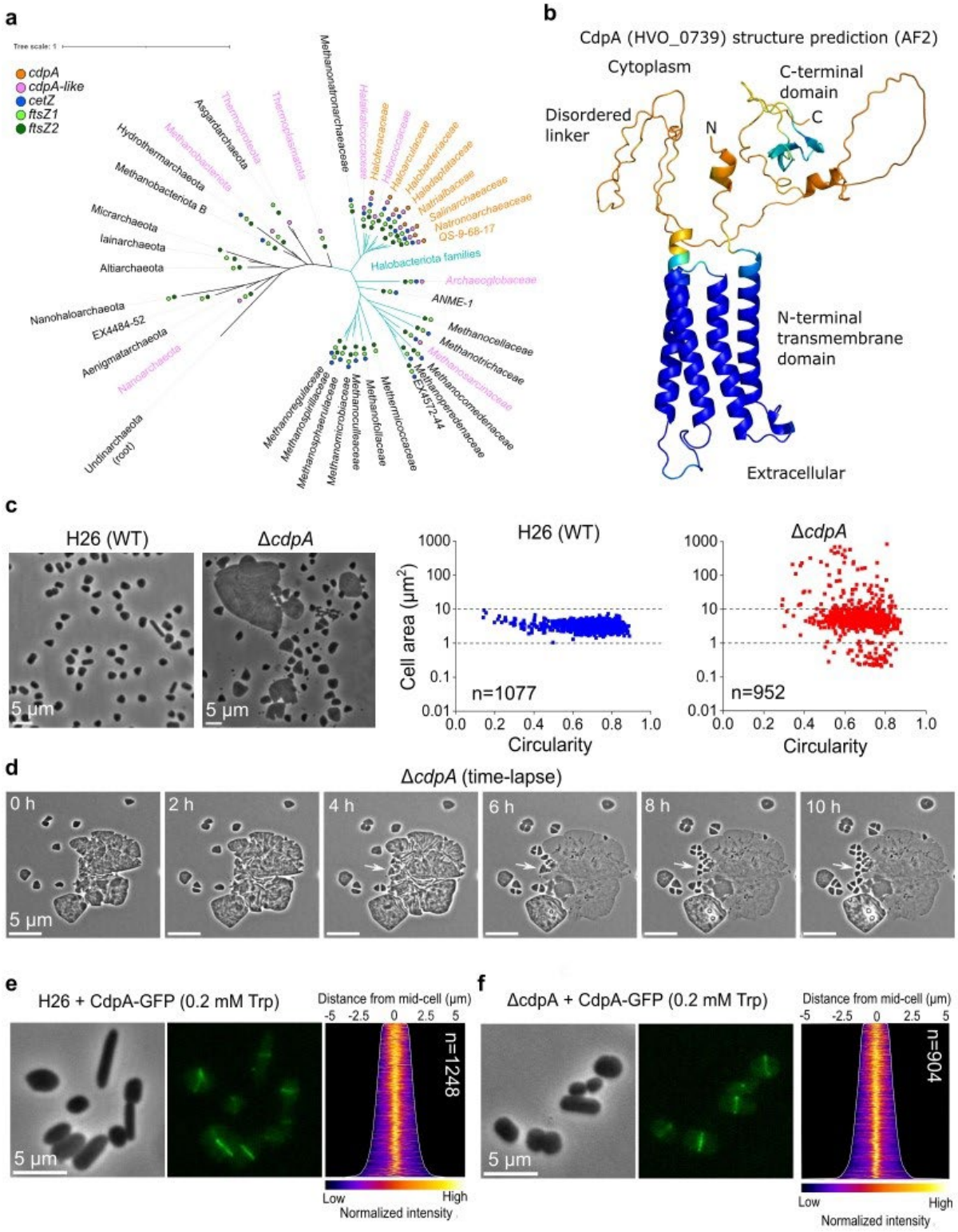

Fig. 1. CdpA is cell division protein in haloarchaea. a, Phylogenetic distribution of CdpA (orange circles), CdpA-like (pink), CetZ (blue), FtsZ1 (light green), and FtsZ2 (dark green) on a schematic reference phylogeny of the Archaea (Genome Taxonomy Database, release 207), expanding on Halobacteriota families. **b,** Alphafold2 prediction of CdpA monomer structure coloured by model confidence (blue - pLDDT > 90%, orange - pLDDT < 50%) and predicted overall membrane topology. **c,**

Phase-contrast microscopy of wild-type (WT) and Δ*cdpA* strains in steady mid-log cultures and the corresponding cell shape analysis. n= number of cells examined over one biologically independent experiment. The data shown is representative of at least two independent experiments. **d,** Live-cell time-lapse images of Δ*cdpA* growing on an agarose media pad and showing cell lysis, fragmentation, and division processes (arrows). **e**, **f,** Phase-contrast and fluorescence micrographs of wild-type cells expressing CdpA-GFP (**e**) and Δ*cdpA* expressing CdpA-GFP (**f**) under control of the *p.tnaA* promoter with 0.2 mM Trp induction. Demographic analysis (righthand panels) showing fluorescence intensity along the long axis ordered by cell lengths, top to bottom. n= number of cells examined over one biologically independent experiment. The data shown in panel d, e, f is representative of at least two independent experiments. All scale bars, 5 µm.

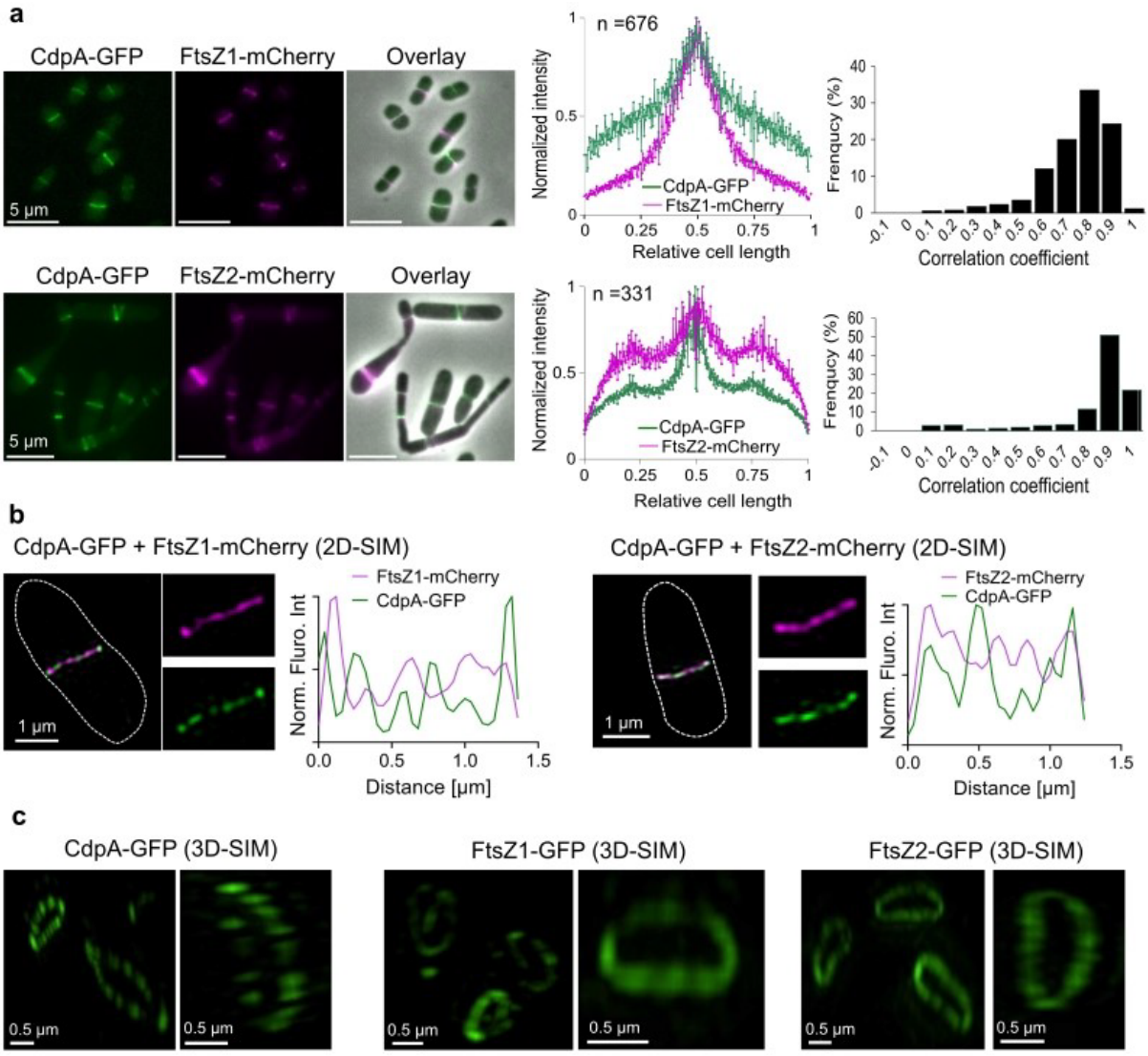

Fig. 2. Sub-cellular and sub-ring localization of CdpA with FtsZ1 or FtsZ2. a, Phase-contrast and fluorescence images of *H. volcanii* strains YL6 (H26 + CdpA-GFP + FtsZ1-mCherry dual expression) and YL7 (H26 + CdpA-GFP + FtsZ2-mCherry dual expression) cultured with 0.2 mM Trp during mid-log growth. The middle graphs show the intensity profile of the fluorescence signal (magenta for mCherry, and green for GFP) by plotting the normalized median intensity perpendicular to the long axis of cells. The right graphs show correlation coefficients plotted as a frequency distribution. n = number of cells examined over one independent experiment. The data shown are representative of at least two independent experiments. Scale bars, 5 µm. **b,** Dual-colour of 2D-SIM images of mid-log *H. volcanii* YL6 and YL7 grown with 0.2 mM Trp. mCh (magenta) and GFP (green) fluorescence was quantified by plotting normalized intensity in the respective channel along the ring band. Scale bars, 1 µm. **c,** 3D-SIM images (xy-tilted) of mid-log *H. volcanii* YL29 (H26 + CdpA-GFP), YL24 (H26 + FtsZ1-GFP), and YL26 (H26 + FtsZ2-GFP) grown with 0.2 mM Trp. Scale bars, 0.5 µm. The data shown in panel b and c are representative of at least two independent experiments.

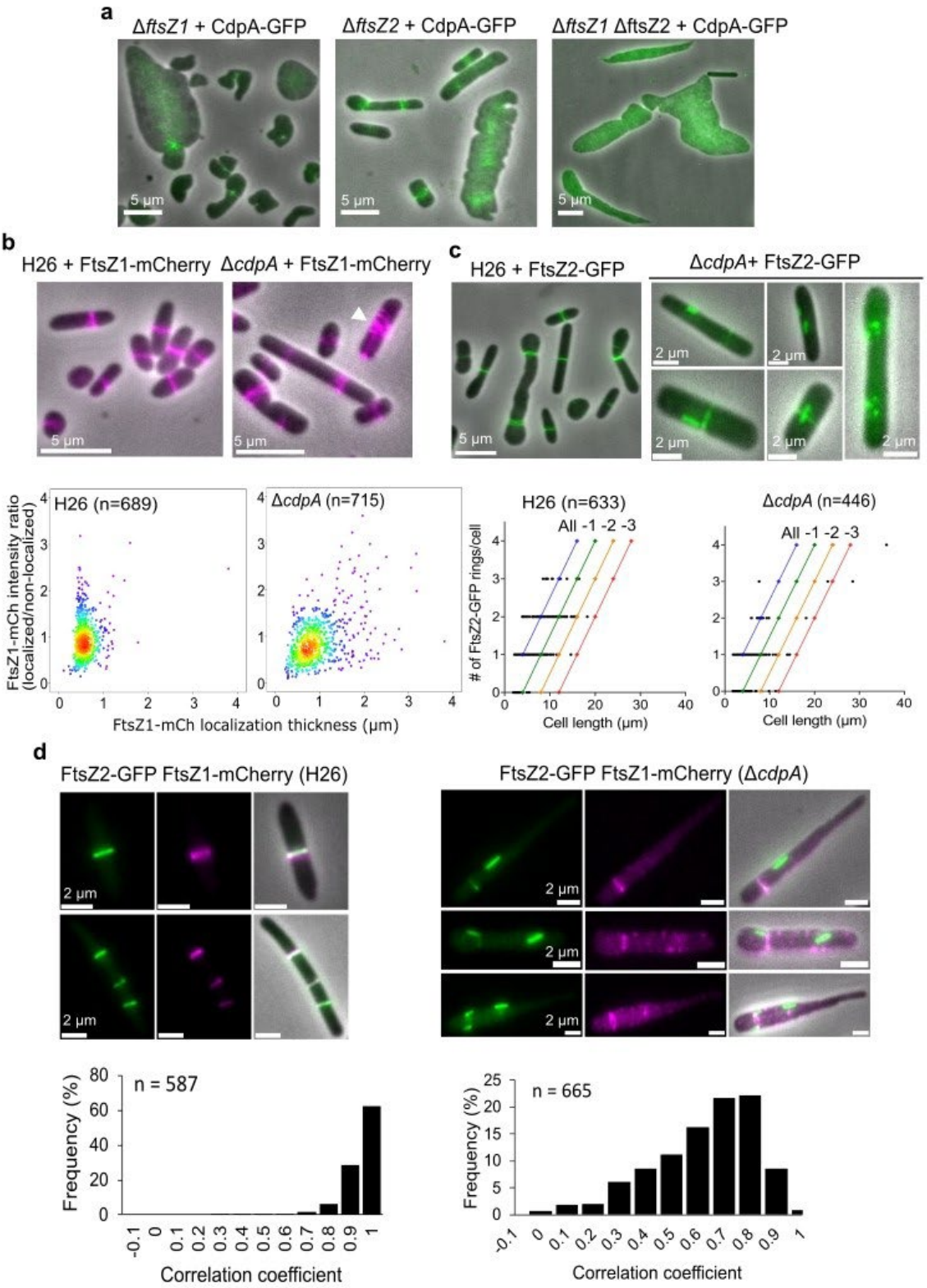

806

807 **Fig. 3. CdpA, FtsZ1 and FtsZ2 show different localization interdependencies and strongly influence**
808 **each other's midcell structures.** All strains were grown in Hv-Cab medium with 0.2 mM Trp, and mid-
809 log cultures were sampled for microscopy. **a,** Phase-contrast and fluorescence composite images of
810 CdpA-GFP in the absence of FtsZ1, FtsZ2, or both. Scale bars, 5 µm. **b,** Left: localization of FtsZ1-mCh
811 in wild-type H26 and Δ*cdpA* backgrounds. The arrowhead indicates a poorly condensed FtsZ1-mCh

812 structure in Δ*cdpA*. Scale bars, 5 µm. The dotplots show quantification of the degree of FtsZ1-mCh
813 localization versus individual localization thickness as a measurement of protein condensation along
814 the long axis in the indicated backgrounds. The data points are coloured with a proximity heatmap. **c,**
815 localization of FtsZ2-GFP in H26 (scale bar, 5 µm) and Δ*cdpA* backgrounds (scale bars, 2 µm). The plots
816 show the number of normal localizations of FtsZ2-GFP versus cell length in the indicated backgrounds.
817 Coloured lines indicate the lengths of cells that have the indicated relative number of localizations per
818 unit length (one ring per ~ 4 um). **d,** Upper: localization of FtsZ1-mCherry and FtsZ2 GFP in H26 and
819 Δ*cdpA* strains. Scale bars, 2 µm, Bottom: correlation coefficient between FtsZ1-mCh and FtsZ2-GFP
820 plotted as a frequency distribution. The majority (97%) of H26 cells had a correlation coefficient of
821 ≥0.8, while only 32% of Δ*cdpA* cells had a correlation coefficient of ≥0.8. For panel b, c, and d, n=
822 number of cells examined over one biologically independent experiment, and the data shown is
823 representative of at least two independent experiments.

824

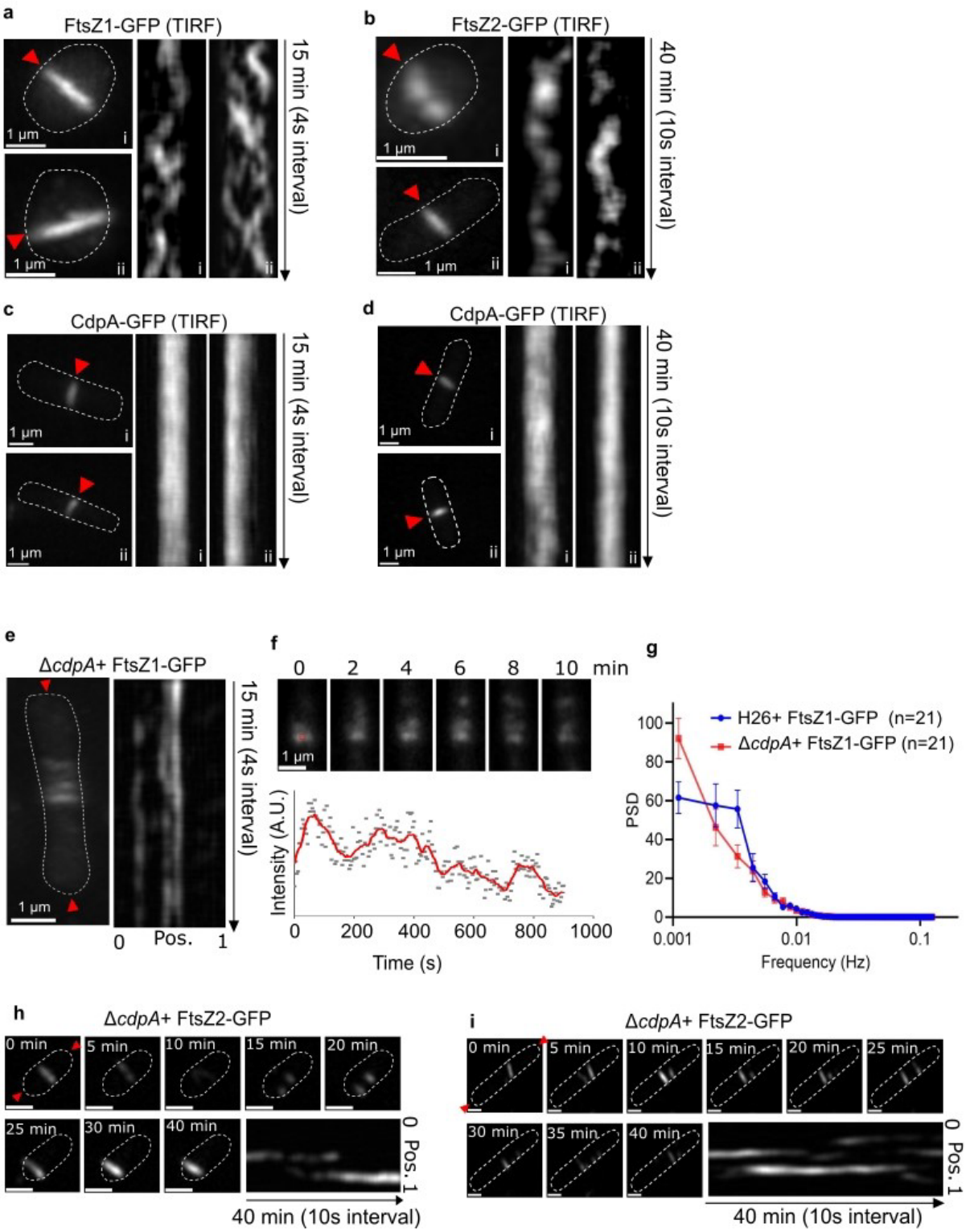

Fig. 4. Division protein localization dynamics and the effect of *cdpA* deletion on FtsZ1 and FtsZ2 movement. Cells were grown in Hv-Cab without tryptophan induction to minimize the expression level of fluorescent fusion proteins. Mid-log cultures were sampled for TRIF imaging. The data shown is representative of at least two independent experiments. **a,** Maximum intensity projections (MIPs) of two representative wild-type H26 cells expressing FtsZ1-GFP (i and ii) are shown on the left, with the corresponding kymographs at positions indicated by red arrows in the MIPs shown on the right. **b,** MIPs of two representative wild-type H26 cells expressing FtsZ2-GFP (i and ii) and their corresponding

833 kymographs. **c-d,** MIPs of wild-type H26 cells expressing CdpA-GFP and their corresponding
834 kymographs with different imaging time-window (4s intervals for 15 mins, panel c; 10s intervals for 40
835 mins, panel d). **e,** MIP of one representative Δ*cdpA* expressing FtsZ1-GFP and its kymograph computed
836 from the intensity along the long axis of cell (between the two red arrows). The relative position (0-1)
837 along the long axis of cell is labelled below the kymograph. **f,** Montages of FtsZ1-GFP dynamics in
838 Δ*cdpA* and the integrated fluorescence time trace for the ROI region (red box) around the centre of
839 ring shown at the start of imaging. The read curve is the moving average (every 5 points) of the raw
840 intensity (grey dots). **g,** The mean power spectral density (PSD) curves (± SEM) of FtsZ1-GFP in wild-
841 type and Δ*cdpA* cells (n=21). **h-i,** Montages of representative FtsZ2-GFP dynamics in two Δ*cdpA* cells
842 and their corresponding kymographs indicate the changes in ring position (h) and orientation (i). All
843 scale bars are 1 µm.

844

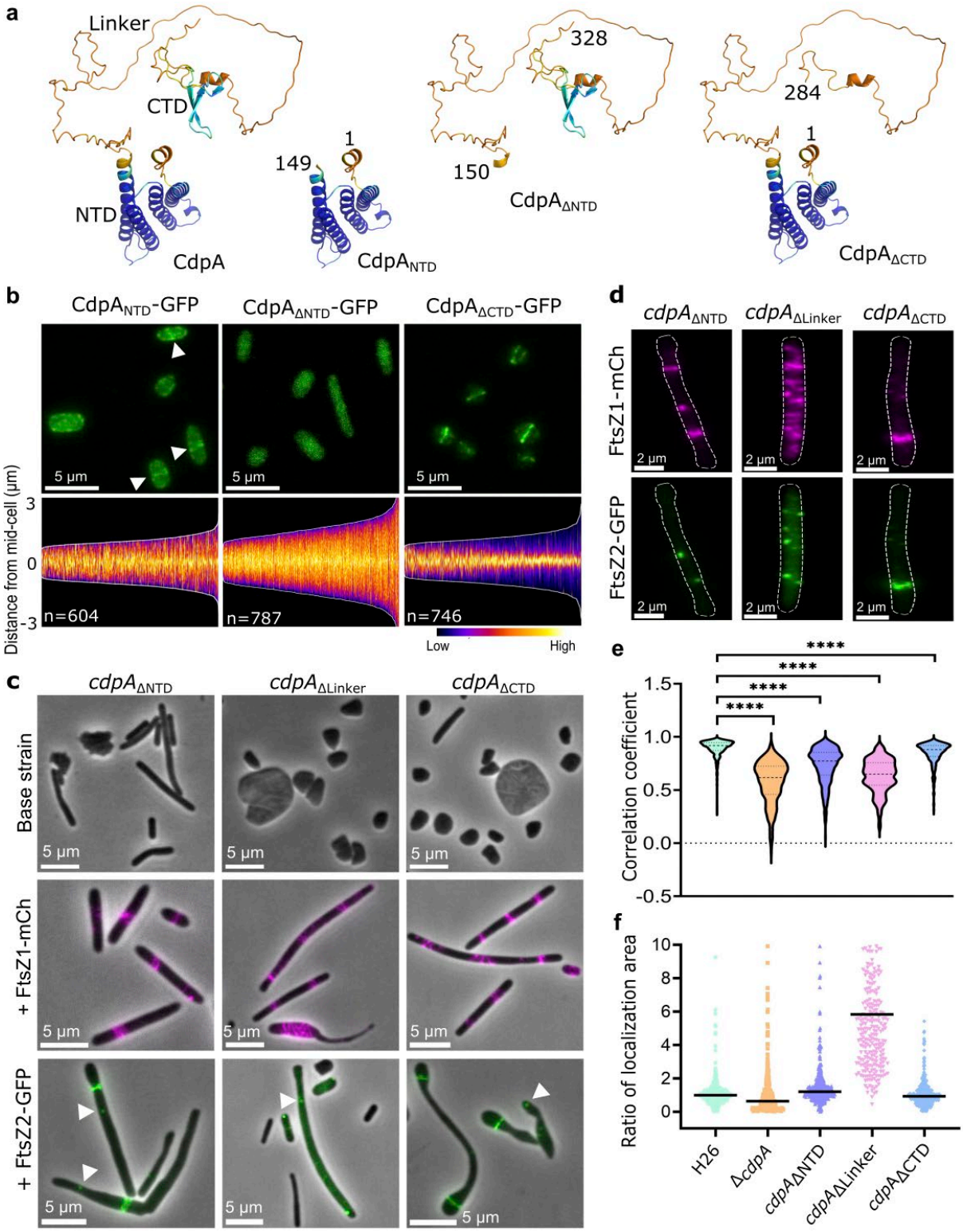

Fig. 5. The three domains of CdpA have differing roles in subcellular localization and assembly of FtsZ1 and FtsZ2. a, Alphafold2 models of CdpA showing domain boundaries of the GFP tagged deletion constructs, including the N-terminal domain (NTD), disordered linker, and C-terminal domain (CTD). **b,** Fluorescence microscopy of H26 wild-type strains expressing the indicated constructs during mid-log growth in Hv-Cab medium with 0.2 mM Trp. Arrows indicate regions of weak mid-cell localization. Scale bars, 5 µm. The lower panels show demographic analyses of fluorescence along the long axis, ordered from shortest to longest cells (left to right). n=number of cells examined over one

853 representative experiment. **c,** Phase-contrast and fluorescence micrographs of the indicated *cdpA*
854 deletion strains producing either FtsZ1-mCh or FtsZ2-GFP, sampled during mid-log phase growth in
855 Hv-Cab + 0.2 mM Trp. Arrows indicate some faint foci of FtsZ2-GFP. **d,** Fluorescence images of the
856 indicated *cdpA* deletion strains co-producing FtsZ1-mCh and FtsZ2-GFP. **e,** Distributions of cellular
857 correlation coefficients and (**f**) ratio of localization area for FtsZ1-mCh:FtsZ2-GFP in the background
858 strains shown below the lower panel. The data shown are representative from one of two
859 independent experiments.

860

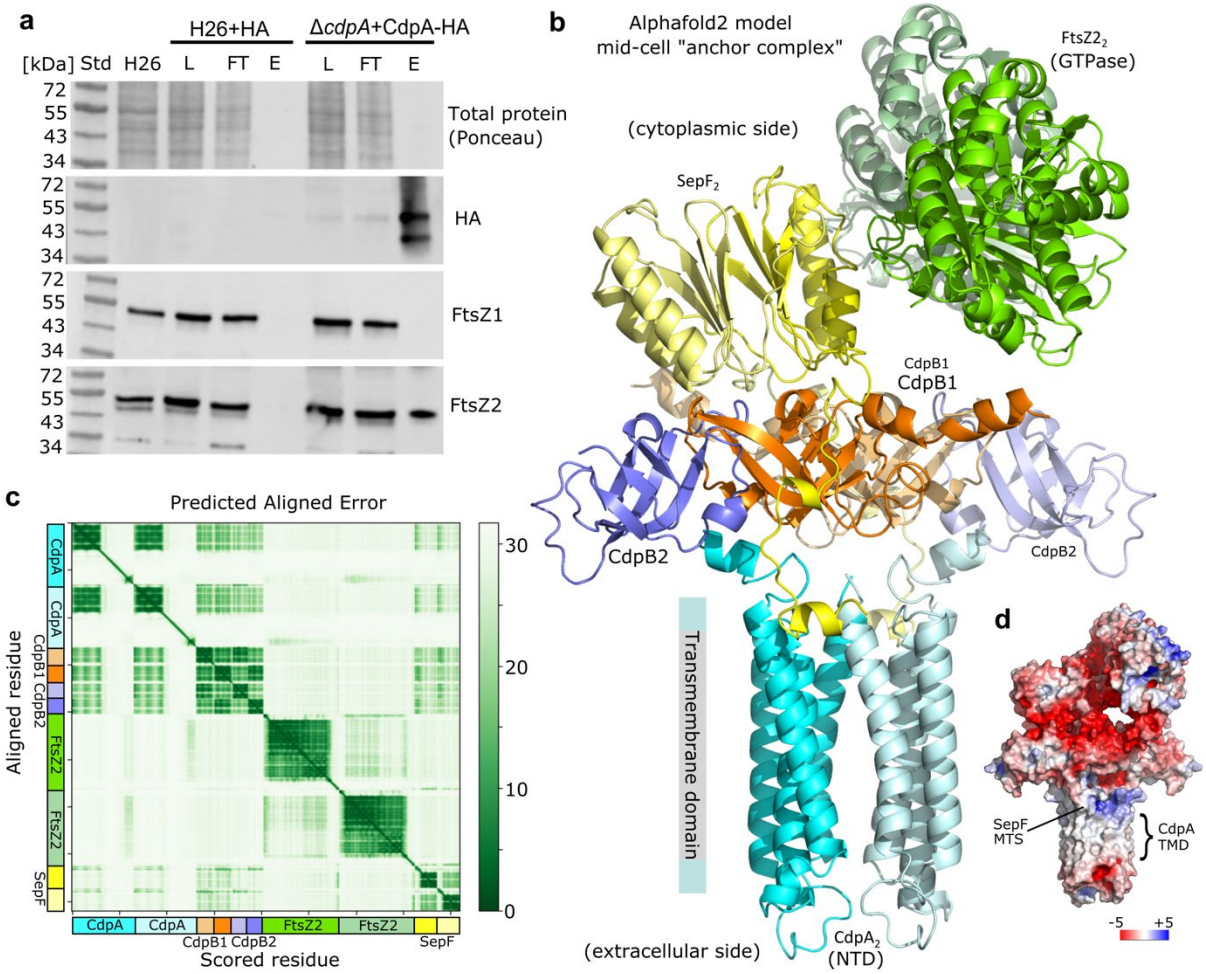

Fig. 6. CdpA is associated with FtsZ2 and other division proteins in a putative membrane anchor complex. a, Western blots of one of three replicate co-immunoprecipitation experiments. The cell lysate (L), unbound protein flow through (FT) and bound protein elution fraction (E) from control (H26 + HA vector only) and Δ*cdpA* + CdpA-HA were analysed by 15% SDS-PAGE and western blotting. The total protein stain (Ponceau S) is shown for the same membrane used for the anti-HA probe, and replicate membranes were probed with anti-FtsZ1 or anti-FtsZ2 as indicated. **b,** Alphafold2 model of the mid-cell anchor complex generated from a sequence input of 2 CdpA, 2 CdpB1, 2 CdpB2, 2 FtsZ2, and 2 SepF. The C-terminal regions of CdpA and the N- and C-terminal extensions of FtsZ2 that are largely disordered are not shown for clarity. **c,** The Alphafold2 predicted aligned error (%) heatmap plot of all input sequences (concatenated), indicating the degree of confidence in pairwise interactions between residues. **d,** The same structure and orientation as in panel b shown with surface electrostatics, indicating the approximate CdpA transmembrane domain (TMD) and SepF membrane targeting sequence (MTS).